Scalable Fabrication of Nanoporous Carbon Fiber Films as Bifunctional Catalytic Electrodes for Flexible Zn-Air Batteries

Qin Liu, Yaobing Wang, Liming Dai,* and Jiannian Yao*

With the rapid development of flexible and wearable optoelectronic devices, there is an urgent demand for flexible high-density energy storage devices as the power source.[1] Tremendous efforts have recently been made to develop flexible lithium-ion batteries and supercapacitors, which, however, are still suffered from not only the low energy density but also the limited cycle life.[2,3] Since metal-air batteries were predicated to possess high energy capacities,[4] they are promising energy storage devices for the next generation of wearable optoelectronics. Of particular interest, Zn-air batteries have received intensive research and development focus because of their high energy density, low cost and safety.[5] However, most of the air-cathodes currently used in Zn-air batteries are heavy and bulky, which seldom meet the specific requirements for flexible Zn-air batteries. Furthermore, it is still a big challenge to develop highly efficient bifunctional electrocatalysts for both oxygen reduction reaction (ORR) and oxygen evolution reaction (OER) to be used in flexible rechargeable Zn-air batteries,[6] though important progresses have recently been made for traditional Zn-air batteries.[5]

Efficient ORR and OER bifunctional catalysts are required for rechargeable Zn-air batteries, in which the kinetics is mainly limited by the key discharge (ORR)/charge (OER) reactions taken places at the air-cathode: $O_2 + 2H_2O + 4e^- \longleftrightarrow 4OH^-$.[7,8] In traditional metal-air rechargeable batteries, Pt and Ir or Ru based catalysts are often used for ORR and OER, respectively, but their high cost, scarcity, and poor durability have impeded the commercialization of rechargeable Zn-air batteries.[9] Recent studies indicated that metal-free heteroatom-doped carbons are promising ORR and OER bifunctional catalysts for rechargeable metal-air batteries, including Zn-air batteries.[7,10,11] With abundant carbon sources and their excellent electrochemical properties and mechanical flexibility,[12] these carbon-based metal-free catalysts could act as desirable low-cost, flexible, and highly active ORR and OER bifunctional catalysts for flexible Zn-air batteries. As far as we are aware, however, the possible use of heteroatom-doped carbon nanomaterials as the metal-free ORR and OER bifunctional catalyst in flexible Zn-air batteries has not been realized. Retaining flexibility and excellent bifunctional electrocatalytic activity for an air-cathode is still challenging for constructing flexible Zn-air batteries.

In this study, we found that the newly-developed nanoporous carbon nanofiber films (NCNFs) with large specific surface area were flexible and showed, when used as the air-cathode in a liquid Zn-air battery operating in ambient air, excellent performance with a high open-circuit voltage (1.48 V), maximum power density (185 mW cm^{-2}), and energy density (776 Wh kg^{-1}). The corresponding rechargeable liquid Zn-air battery exhibited a small charge-discharge voltage gap (0.73 V @ 10 mA cm^{-2}) and high reversibility (initial round-trip efficiency = 62%) and stability (voltage gap increased ≈0.13 V after 500 cycles). More interestingly, flexible all-solid-state rechargeable Zn-air batteries with the NCNF air-cathode displayed an excellent mechanical and cycling stability with a low overpotential (a high discharge and low charge voltage of ≈1.0 and ≈1.78 V @ 2 mA cm^{-2}, respectively) as well as a long cycle life (6 h, which can be recharged by mechanical replacement of the Zn anode) even under repeated bending conditions. Four of the newly-developed flexible all-solid-state rechargeable Zn-air batteries based on the NCNF air-cathode were integrated in series to power commercial light-emitting diodes (LED, 3 V) worn on a human hand, exemplifying the feasibility for practical applications as flexible power sources in wearable optoelectronics.

The NCNFs were prepared by high-temperature pyrolysis of electrospun polyimide (PI) film under Ar atmosphere (**Figure 1**a). PI is a kind of promising engineering polymer with outstanding thermal, mechanical, and dielectrics properties, and can be scaled-up to produce large-area homogenous films by solution casting or nanoprous fiber films by electrospinning (Figure S1a, Supporting Information).[13] After pyrolysis, the yellow PI film turned into black while its structural integrity was largely retained (Figure 1a; Figure S1b, Supporting Information). The as-prepared NCNF-1000 (pyrolyzed at

Dr. Q. Liu, Prof. Y. Wang
Key Laboratory of Design and Assembly of Functional Nanostructures
Fujian Provincial Key Laboratory of Nanomaterials
Fujian Institute of Research on the Structure of Matter
Chinese Academy of Sciences
Fuzhou 350002, China
E-mail: wangyb@fjirsm.ac.cn
Prof. L. Dai
Center of Advanced Science and Engineering for Carbon (Case 4Carbon)
Department of Macromolecular Science and Engineering
Case Western Reserve University
10900 Euclid Avenue, Cleveland, OH 44106, USA
E-mail: liming.dai@case.edu
Prof. J. Yao
Beijing National Laboratory for Molecular Sciences
Institute of Chemistry
Chinese Academy of Sciences
Beijing 100190, China

DOI: 10.1002/adma.201506112

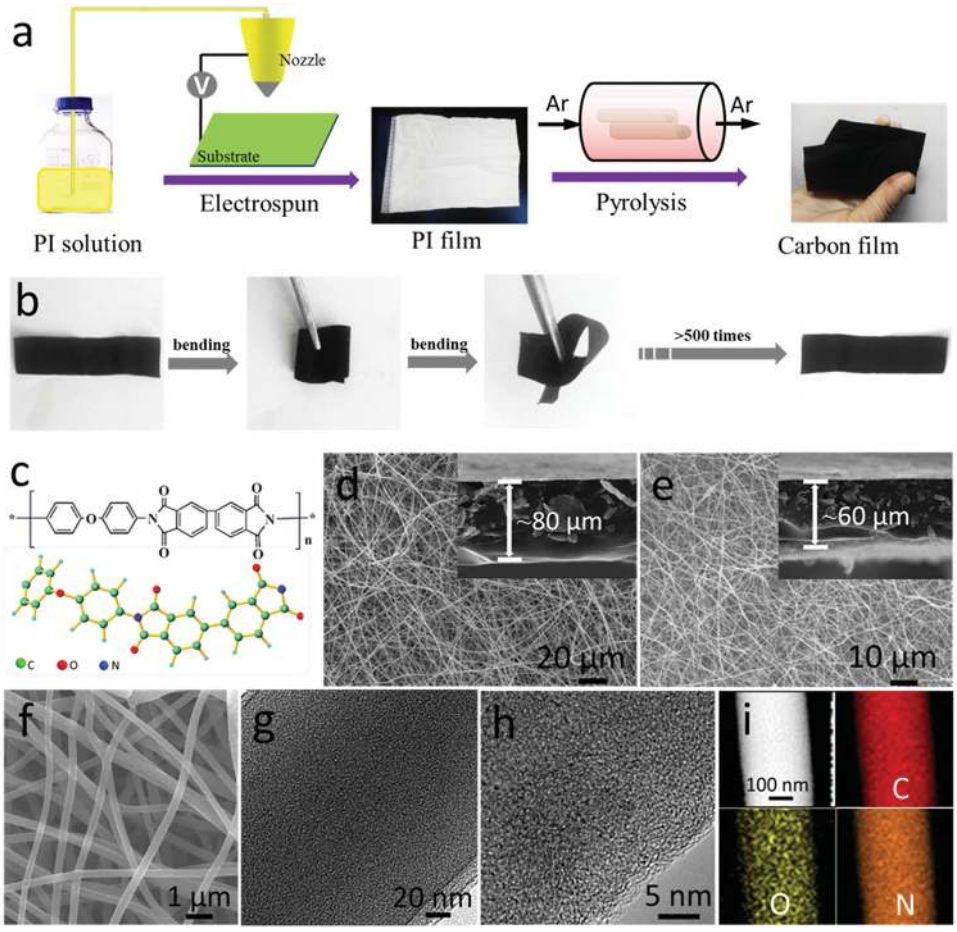

Figure 1. a) Schematic representation of the fabrication procedure toward the NCNF. b) Photographs of the resultant flexible NCNF. c) Chemical structure of PI polymer. SEM images of d) the pristine PI film and e,f) NCNF-1000. g,h) HRTEM, i) STEM images and corresponding elemental mapping images of C, O, N of NCNF-1000.

1000 °C) is highly flexible (Figure 1b) and mechanically strong with a tensile strength of 1.89 MPa and a tensile modulus of 0.31 GPa (Figure S2, Supporting Information), presumably arising, at least partially, from the polar interactions associated with the constituent oxygen, nitrogen, and/or hydrogen atoms along the polymer backbone (Figure 1c) before and after the carbonization. The scanning electron microscopy (SEM) images (Figure 1d,e) and atomic force microscopy (AFM) images (Figure S3, Supporting Information) show a typical 3D randomly entangled fibrous network structure for the electrospun PI film before and after pyrolysis. The pyrolysis caused a reduction in the film thickness from about 80 μm for the electrospun PI film to about 60 μm for the NCNF-1000 (insets of Figure 1d,e). Enlarged views of the NCNF-1000 on SEM (Figure 1f) and high-resolution transmission electron microscope (HRTEM, Figure 1g) show a diameter of ≈300 nm for the constituent fibers. The observed mechanical flexibility could be directly attributed to the open-pore network structure of the NCNF, in which the free space between the constituent fibers can effectively attenuate the bending stress without damaging the fibers.[14] A HRTEM image of a single NCNF-1000 fiber under higher magnification is given in Figure 1h, which shows an amorphous carbon structure consisting of randomly orientated graphitic domains. The energy-dispersive X-ray (EDX) spectrum confirms the presence of C, N, O elements (Figure S4, Supporting Information) while the STEM images and the corresponding elemental mapping images reveal a uniform distribution for C, N and O atoms within the NCNF-1000 fiber (Figure 1i).

The low graphitization degree with a defective structure in the NCNF fibers observed by HRTEM (Figure 1h) was further confirmed by our Raman spectra (**Figure 2**a) with a relatively high $I_{D\ (1345\ cm^{-1})}/I_{G\ (1595\ cm^{-1})}$ ratio (≈1.0) and the corresponding X-ray diffraction (XRD) patterns (Figure 2b) with a broad (002) diffraction peak at 23.4°. The chemical compositions of the NCNF were investigated by elemental analysis (EA) and X-ray photoelectron spectroscopy (XPS). As expected, the XPS survey spectra show three peaks corresponding to C1s, O1s, and N1s in the NCNF (Figure S5a, Supporting Information). Compared to the C1s peak, both the nitrogen and oxygen contents decreased with increasing pyrolysis temperature with an atomic N content of 2.36% for NCNF-900, 1.55% for NCNF-1000, and 0.96% for NCNF-1100 (see also Table S1 in the Supporting Information). The curve-fitted high-resolution XPS N1s spectra given in Figure 2c show three distinguished nitrogen species, including pyridinic-N (398.5 eV), pyrrolic-N (400.2 eV), and graphitic-N

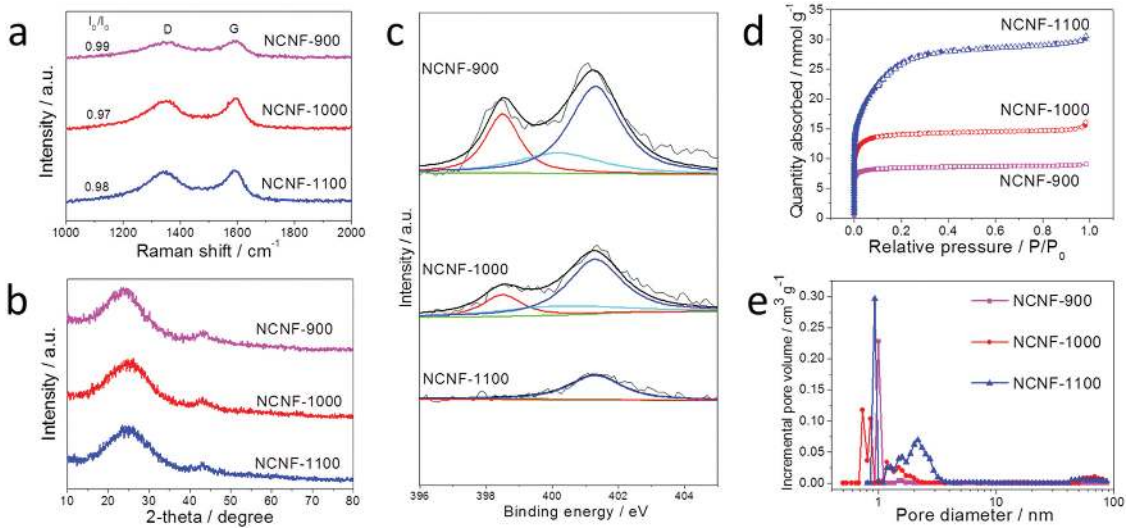

Figure 2. a) Raman spectra, b) XRD patterns, c) curve-fitted high-resolution XPS N1s spectra, d) N_2 adsorption-desorption isotherms, and e) pore size distribution curves for NCNF-900, NCNF-1000, and NCNF-1100.

(401.3 eV), whose contents also changed with the pyrolysis temperature. As shown in Figure 2c and Figure S5b (Supporting Information), the graphitic-N became the dominant component with increasing pyrolysis temperature, due, most probably, to the decomposition of unstable pyridinic-N and pyrrolic-N into the graphitic-N.[15] Due to the stable aromatic structure of PI, the removed nitrogen occurs over a high temperature of ≈550–800 °C in the form of nitrogen-containing gaseous compounds, such as HCN and NH_3 (Figure S6, Supporting Information), which could be served as the source for N-doping and activation of the resultant carbon material.[16] In order to enhance the likelihood of N-doping and in situ activation,[17] we have deliberately increased the residence time for the evolved gases (HCN, NH_3, H_2O) by reducing the flow rate of the inert carrying gas in this study. In addition to the N-doping, the NCNFs also contain oxygen-containing groups, mainly ketonic C═O and C—O (Figure S5c, Supporting Information), to introduce defect sites into the adjacent carbon atoms.[18]

We also performed N_2 adsorption measurements to determine the specific surface area and pore structure of the NCNFs. It was found that the BET surface area was 756 m^2 g^{-1} for NCNF-900, 1249 m^2 g^{-1} for NCNF-1000, and 2149 m^2 g^{-1} for NCNF-1100 (Table S2, Supporting Information). All the NCNF samples show a typical type I pattern for the N_2 adsorption with a steep climbing increase at low relative pressure ($P/P_O < 0.1$), implying the presence of microporous structures (Figure 2d). This can be further confirmed from the pore diameter distribution plots (Figure 2e), which show a sharp peak at <2 nm. Clearly, therefore, flexible N-doped carbon nanoprous fibrous films with a large surface area and a 3D network structure have been synthesized by pyrolysis of polymer films consisting of electrospun nitrogen-containing PI nanofibers.

The N-doping in coupled with the 3D nanoporous carbon network structure makes the NCNF attractive as metal-free electrocatalysts.[8] In this context, the high electrical conductivities of the NCNFs (41-150 S m^{-1}, depending on the pyrolysis temperature) measured by four-probe method (Table S1, Supporting Information) provide an additional advantage for electrocatalytic application.[3] To evaluate the electrocatalytic performance of the NCNF, we performed cyclic voltammetry (CV) and linear sweep voltammetry (LSV) measurements in 0.1 M KOH solution. As shown in **Figure 3**a, a cathodic peak for ORR is observed for the NCNF-1000 in O_2-saturated KOH solution, but not in N_2-saturated KOH solution, as is the case with Pt/C. The oxygen reduction peak of NCNF-1000 appears at about 0.80 V, which is slightly less positive than that of commercial Pt/C (0.83 V). However, the reduction current density for NCNF-1000 (1.39 mA cm^{-2}) is obviously higher than that of Pt/C (1.09 mA cm^{-2}). Decreasing pyrolysis temperature to 900 °C or increasing to 1100 °C would result to decreased ORR performance in the terms of reduction potential and current density (Figure S7a,d, Supporting Information), as a result of the combined effects of the surface area and dopant content. Generally speaking, both a higher surface area and higher N-doping level could lead to a larger catalytic activity.[11] By increasing the pyrolysis temperature from 900 to 1000 °C, the surface area of the NCNF increased from 756 to 1249 m^2 g^{-1} (Table S2 Supporting Information), whereas the N-doping level decreased from 2.36 to 1.55% (Table S1, Supporting Information).

Figure 3b reproduces the LSV curves measured on a rotating disk electrode (RDE) at a rotating speed of 1600 rpm in an aqueous solution of 0.1 M KOH, with a comparable onset potential (≈0.97 V) for NCNF-1000 to that of Pt/C, along with a higher limiting current density for NCNF-1000 (4.7 mA cm^{-2}) than that of Pt/C (4.4 mA cm^{-2}), NCNF-900 (3.3 mA cm^{-2}), and NCNF-1100 (3.4 mA cm^{-2}). These results indicate that NCNF-1000 is the best ORR electrocatalyst and even better than Pt/C. RDE measurements at various rotating speeds were also performed to gain insights into the ORR kinetics (Figure 3c; Figure S7b,e,h, Supporting Information). The current density shows a linear increase with increasing rotating speed, implying a first-order reaction toward oxygen reduction (Figure S7c,f,i, Supporting Information). The number of electron transfer per

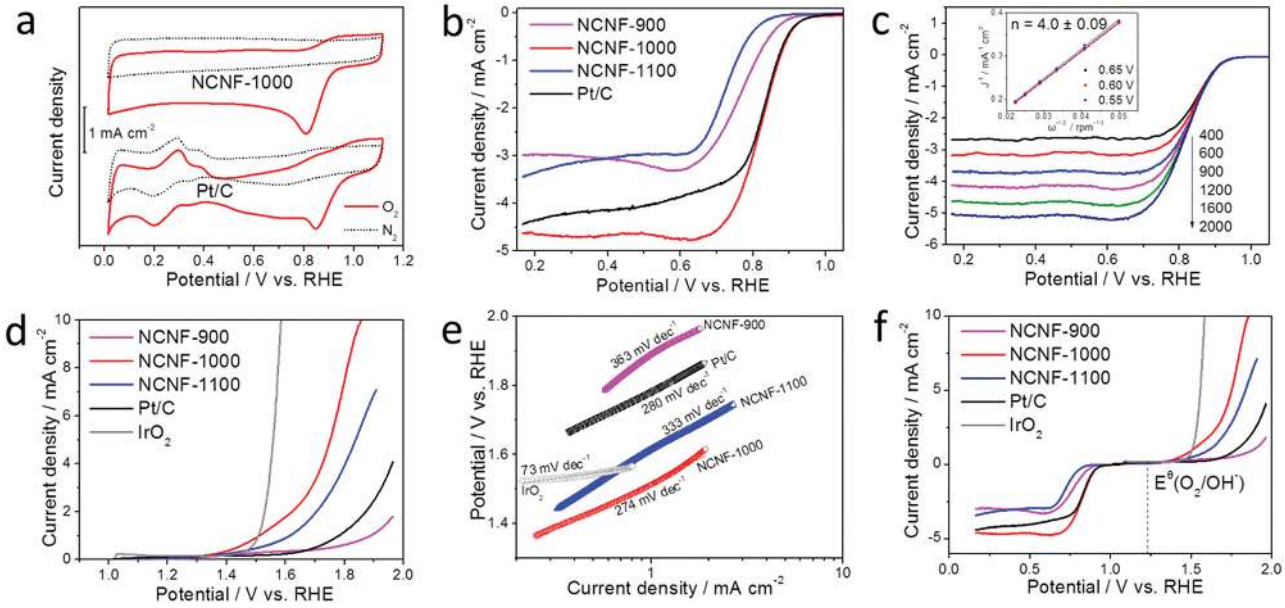

Figure 3. a) CV curves of NCNF-1000 and Pt/C, in O_2-saturated (solid line) and N_2-saturated (dotted line) 0.1 M KOH. b) LSV curves of different catalysts for ORR in O_2-saturated at 1600 rpm. c) LSV curves of NCNF-1000 for ORR at different rotating speeds, and the inset is K-L plots of NCNF-1000 at different potentials including the calculated number of electron transfer (n) per O_2. d) LSV curves of different catalysts for OER at 1600 rpm in 0.1 M KOH. e) Tafel slopes derived from (d). f) LSV curves of different catalysts for both ORR and OER in 0.1 M KOH at 1600 rpm (scan rate 5 mV s^{-1}). The catalyst loading was 0.1 mg cm^{-2} for all catalysts.

O_2 for NCNF-1000 was calculated from Koutecky–Levich (K-L) plots (see inset of Figure 3c) to be about 4 in the potential range from 0.55 to 0.65 V, comparable to that of Pt/C (Figure S7i, Table S3, Supporting Information), suggesting an effective four-electron pathway for ORR.

The OER catalytic activities of the NCNF and Pt/C were also characterized by LSV curves measured on RDE at 1600 rpm. As shown in Figure 3d, the NCNF-1000 displays a lower onset potential (1.43 V) and higher catalytic current than Pt/C. Compared to the state-of-the-art IrO_2, the NCNF-1000 also exhibits a lower onset potential, though a lower catalytic current density over a large potential range above the onset potential. Meanwhile, the NCNF-1000 electrode exhibits a smaller Tafel slope (274 mV/decade) than that of Pt/C, suggesting a better kinetic process (Figure 3e). Figure 3f clearly shows excellent ORR and OER bifunctional activities for the NCNF-1000, which can be judged by the potential difference between OER and ORR (i.e., $\triangle E = E_{j=10} - E_{1/2}$, with the OER potential being taken at a current density of 10 mA cm^{-2} while the ORR potential being taken at half-wave). The lower the $\triangle E$ value is, the better bifunctional activity the catalyst has.[19] Table S4 (Supporting Information) shows that the $\triangle E$ value for NCNF-1000, along with its other performance parameters, are comparable with other reported state-of-the-art ORR and OER bifunctional electrocatalysts, including those based on metal oxides.

The possible catalytic active sites for ORR and OER were elucidated. It is known that the doped N atom in carbon framework can introduce uneven charge distribution and make the nearby carbon atoms positively charged, due to the electronic affinity of the nitrogen atom.[7a,10a] The positively charged carbon atoms would favor the oxygen adsorption, thus promoting ORR. Thus, the positively charged carbon atoms introduced by adjacent nitrogen are considered as the catalytic active sites for ORR. For the OER process, the adsorption of OH^- on catalyst surface become easily, as well as the transfer of possible intermediates such as O_2^{2-} and O^{2-}, resulting in improved OER activity.[20] In addition to the doped nitrogen atoms, the existence of oxygen atoms confirmed by high resolution XPS O1s spectra (Figure S5c, Supporting Information) and element mapping (Figure 1i) might also introduce positively charged carbon atoms as active sites for OER, due to the larger electronegativity of oxygen (3.44) than that of carbon atoms (2.55).[18][20b] It is probable that the dual active sites originating from nitrogen and oxygen atoms are responsible for the electrocatalytic activity toward OER. In summary, we consider that the active sites resulted by nitrogen doping are responsible for the excellent ORR activity, while the dual active sites originating from nitrogen and oxygen doping are probably responsible for the good OER activity in our NCNF materials.

To evaluate the utility of NCNF as catalyst in Zn-air batteries, a primary Zn-air battery was first built, in which a zinc plate was used as the anode and the NCNF-1000 catalyst-loaded porous electrode as the air-cathode (Figure S8, Supporting Information). The air-cathode was prepared by rolling carbon black mixed with polytetrafluoroethylene (PTFE) on one side of a stainless steel mesh (mesh 40 × 40, type 304) to be the gas diffusion layer, followed by coating the NCNF-1000 catalyst slurry on the other side of the stainless steel mesh (Figure S9, Supporting Information). **Figure 4**a reproduces the polarization and power density curves for the liquid primary Zn-air batteries with the NCNF catalysts. The open-circuit voltage (OCV), maximum power density of the Zn-air battery using NCNF-1000 catalyst were determined to be as high as 1.48 V and 185 mW cm^{-2}, respectively, exceeding those of the Pt/C-based

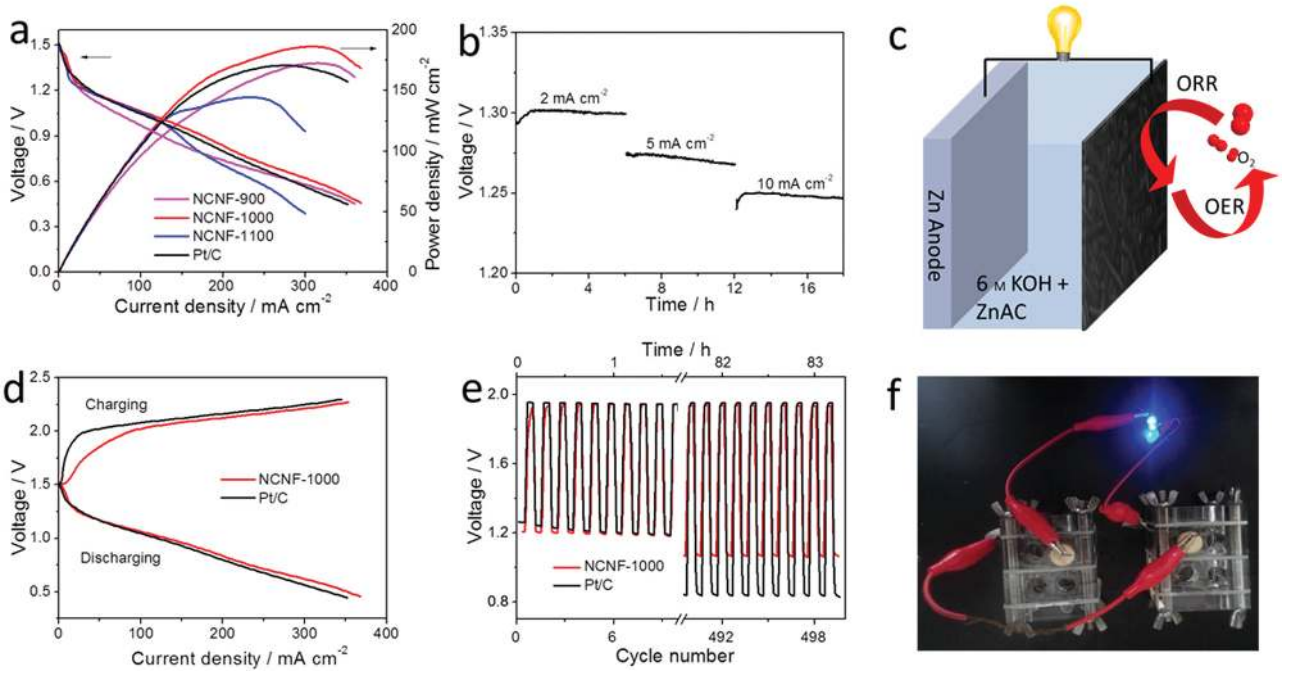

Figure 4. a) Polarization and power density curves of the primary Zn-air batteries with different catalysts. b) Galvanostatic discharge curves of the primary Zn-air battery with NCNF-1000 as catalyst at different current densities, which was normalized to the area of air-cathode. c) Schematic representation of the rechargeable Zn-air battery. d) Charge and discharge polarization curves. e) Galvanostatic discharge–charge cycling curves at 10 mA cm^{-2} of rechargeable Zn-air batteries with the NCNF-1000 and Pt/C as catalyst, respectively. f) Photograph of a blue LED (≈3.0 V) powered by two liquid Zn-air batteries with the NCNF-1000 air-cathode connected in series.

counterpart. The galvanostatic discharge voltage plateaus decreased with increasing current densities (Figure 4b). At the discharge current densities of 5 and 10 mA cm^{-2}, the battery with the NCNF-1000 air-cathode showed voltage plateaus of ≈1.27 and ≈1.24 V, respectively, with specific capacities of 660 and 626 mAh g^{-1} when normalized to the weight of consumed zinc electrode (Figure S10a, Supporting Information). The corresponding energy densities were 838 and 776 Wh kg^{-1}, respectively. These values are comparable or even higher than other reported results[5f,9e,21] due, at least partially, to the large surface area of the NCNF-1000. Furthermore, no obvious voltage drop was observed after discharge for about 16 h (Figure S10b, Supporting Information), indicating an excellent durability for NCNF-1000 toward ORR.

We also constructed a rechargeable Zn-air battery (Figure 4c) with the same configuration as that of the primary counterpart (Figure S8, Supporting Information), but using 6 M KOH with 0.2 M zinc acetate as the electrolyte. Figure 4d shows the discharge and charge polarization curves for Zn-air batteries with NCNF-1000 as the ORR and OER bifunctional catalyst in comparison to Pt/C. Compared to a Zn-air battery with a Pt/C air-cathode, a slightly lower charge-discharge voltage gap was observed for the Zn-air battery with the NCNF-1000 air-cathode, indicating a better rechargeability. When cycled at the constant current density of 10 mA cm^{-2}, the Zn-air battery based on the NCNF-1000 air-cathode produced an initial charge potential of 1.93 V and discharge potential of 1.20 V, with a small voltage gap of 0.73 V and a high round-trip efficiency of 62% (Figure 4e). After 500 cycles (about 83 h), the NCNF-1000 air-cathode showed a slight performance loss with a small increase in the voltage gap by 0.13 V, whereas Pt/C demonstrated a significantly higher increase in the voltage gap (0.38 V) under the same condition. The observed performance decay for the NCNF-1000 is due, most probably, to the inevitable exposure to positive potential during OER to cause the carbon catalyst oxidization and the loss of active sites.[9c,21] The Pt/C air-cathode was suffered from not only the carbon support corrosion but also the subsequent detachment of Pt nanoparticles from the carbon support and particle agglomeration. Therefore, the Zn-air battery using the NCNF-1000 air-cathode showed a much better cycling durability than that of its counterpart based on the Pt/C, and many other state-of-the-art Zn-air batteries reported to date (Table S5, Supporting Information). Multiple Zn-air batteries with the NCNF-1000 air-cathode thus prepared can be integrated into circuits to meet specific energy/power needs for various applications, as exemplified by Figure 4f showing two series-connected Zn-air batteries based on the NCNF-1000 air-cathode being used to power a blue light-emitting diode (LED, 3.0 V) with an excellent operation stability (e.g., without obvious change in brightness for 12 h).

To demonstrate potential applications in flexible/wearable optoelectronics, we have further developed flexible all-solid-state Zn-air batteries composed of a free-standing NCNF-1000 air-cathode, zinc foil anode, alkaline poly(vinyl alcohol) (PVA) gel electrolyte, and pressed (for strengthen conductivity) nickel foam current collector (**Figure 5**a,b; Figure S11, Supporting Information). Compared to those liquid batteries discussed above, the all-solid-state battery displayed a relatively poorer charge–discharge performance due to the poor ionic conductivity of the PVA gel electrolyte and the high contact resistance.

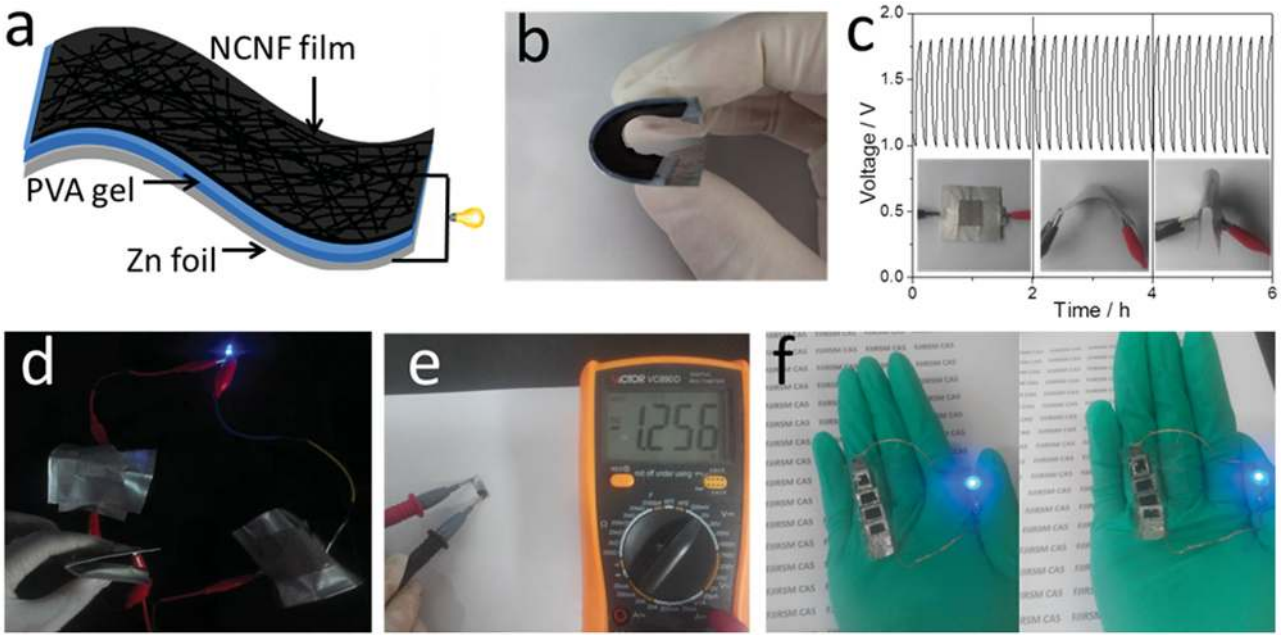

Figure 5. a) Schematic represention and b) photograph of the all-solid-state rechargeable Zn-air battery. c) Galvanostatic discharge-charge cycling curve at 2 mA cm^{-2} for the all-solid-state rechargeable Zn-air battery with NCNF-1000 as catalyst, applying bending strain every 2 h. d) Photograph of a blue LED (≈3.0 V) powered by three all-solid-state Zn-air batteries in series. e) Photograph of an all-solid-state Zn-air micro battery with an open circuit voltage of 1.26 V. f) Photographs of a blue LED (3.0 V) powered by four all-solid-state Zn-air micro batteries in series.

However, the newly-developed all-solid-state battery exhibited a good flexibility and cycling stability. As shown in Figure 5c, the all-solid-state battery exhibited stable charge (1.78 V) and discharge (1.0 V) potentials at the current density of 2 mA cm^{-2} for 6 h even when the device was bended to a large angle or folded back to front. Furthermore, no apparent changes of the structure and morphology of NCNF-1000 were observed, after 48 cycles (Figure S12, Supporting Information). The calculated specific capacity and energy density of this all-solid-state battery were 378 mAh g^{-1} and ≈378 Wh kg^{-1}, respectively. Three all-solid-state Zn-air batteries integrated into a series circuit could be used to power a blue LED (≈3.0 V), even under the bending condition (Figure 5d).

Apart from the good flexibility, the electrode design offers additional advantages to eliminate the polymer binder and to simplify the fabrication procedure, compared to the reported flexible Zn-air batteries.[5c] Unlike the air-electrodes prepared by conventional drop-casting method, our NCNF electrode having the 3D nanoporous carbon network structure with a large specific surface area can provide short and fast electron/ion paths and abundant channels for gas diffusion. Besides, the robustly flexible and highly conductive NCNF could be used as a self-supporting electrode and/or current collector to minimize the cell size and cost. Figure 5e shows an all-solid-state Zn-air micro battery without binder and current collector, in which the carbon film was placed next to zinc foil coated by PVA gel and exposed to ambient air. A high OCV of 1.26 V was obtained. Series-connected all-solid-state Zn-air micro batteries could be used to power a blue LED (3.0 V) without obvious performance decay even when the cells were bent by human hand movements (Figure 5f; Figure S13, Supporting Information), indicating possibilities for the all-solid-state Zn-air micro batteries based on the NCNF to be used in flexible and wearable optoelectronic devices.

In summary, we have developed a facile method for scalable synthesis of nanoporous carbon nanofiber films (i.e., NCNFs) simply by high-temperature pyrolysis of electrospun polyimide fiber films. The resultant NCNFs are flexible and possess a large specific surface area (1249 m^2 g^{-1}), high electrical conductivity (147 S m^{-1}), moderate tensile strength (1.89 MPa), and tensile modulus (0.31 GPa). They were revealed to show excellent bifunctional electrocatalytic activities toward ORR (onset potential = 0.97 V vs RHE; limiting current density = 4.7 mA cm^{-2}) and OER (onset potential = 1.43 V vs RHE, potential = 1.84 V @ 10 mA cm^{-2}). Primary liquid Zn-air batteries based on the NCNF air-cathode were demonstrated to show high maximum power density of 185 mW cm^{-2}, specic capacity of 626 mAh g^{-1}, and energy density of 776 Wh kg^{-1}. Furthermore, rechargeable liquid Zn-air batteries based on the NCNF air-cathode were also constructed to exhibit a small charge–discharge voltage gap (≈0.73 V @ 10 mA cm^{-2}) and high reversibility (initial round-trip efficiency = 62%) and stability (voltage gap increased ≈0.13 V after 500 cycles), outperformed most of the recently reported Zn-air batteries. More importantly, flexible all-solid-state rechargeable Zn-air batteries with the NCNF air-cathode were also demonstrated to exhibit a high discharge voltage (≈1.0 V @ 2 mA cm^{-2}), low charge voltage (≈1.8 V @ 2 mA cm^{-2}), high energy density of 378 Wh kg^{-1}, along with an excellent mechanical and cycling stability. These flexible Zn-air batteries could be integrated as the power source into flexible and wearable optoelectronics (e.g., LEDs) and many other systems.

Supporting Information

Supporting Information is available from the Wiley Online Library or from the author.

Acknowledgements

This work was supported by the One Hundred Talents Program of the Chinese Academy of Sciences, the National Natural Science Foundation of China (Grant Nos. 51342009 and 21501173), the Natural Science Foundation of Fujian Province (Grant No. 2014J05027), Science and technology planning project of Fujian province (Grant No. 2014H2008), and NSF (Grant No. CMMI-1400274). The authors are grateful to Prof. Haoqing Hou and Prof. Shuiliang Chen, at the Jiangxi Normal University, for their assistance in some material characterization.

Received: December 8, 2015
Revised: January 6, 2016
Published online: February 23, 2016

[1] a) X. Wang, X. Lu, B. Liu, D. Chen, Y. Tong, G. Shen, *Adv. Mater.* **2014**, *26*, 4763; b) A. Sekiguchi, F. Tanaka, T. Saito, Y. Kuwahara, S. Sakurai, D. N. Futaba, T. Yamada, K. Hata, *Nano Lett.* **2015**, *15*, 5716.

[2] a) Y. J. Nam, S.-J. Cho, D. Y. Oh, J.-M. Lim, S. Y. Kim, J. H. Song, Y.-G. Lee, S.-Y. Lee, Y. S. Jung, *Nano Lett.* **2015**, *15*, 3317; b) G. Zhou, F. Li, H.-M. Cheng, *Energy Environ. Sci.* **2014**, *7*, 1307; c) M. Koo, K.-I. Park, S. H. Lee, M. Suh, D. Y. Jeon, J. W. Choi, K. Kang, K. J. Lee, *Nano Lett.* **2012**, *12*, 4810; d) P. Yang, Y. Ding, Z. Lin, Z. Chen, Y. Li, P. Qiang, M. Ebrahimi, W. Mai, C. P. Wong, Z. L. Wang, *Nano Lett.* **2014**, *14*, 731; e) X. Cao, B. Zheng, W. Shi, J. Yang, Z. Fan, Z. Luo, X. Rui, B. Chen, Q. Yan, H. Zhang, *Adv. Mater.* **2015**, *27*, 4695.

[3] L. Li, S. Peng, H. B. Wu, L. Yu, S. Madhavi, X. W. Lou, *Adv. Energy Mater.* **2015**, DOI: 10.1002/aenm.201500753.

[4] a) Y. Li, H. Dai, *Chem. Soc. Rev.* **2014**, *43*, 5257; b) J.-S. Lee, S. Tai Kim, R. Cao, N.-S. Choi, M. Liu, K. T. Lee, J. Cho, *Adv. Energy Mater.* **2011**, *1*, 34.

[5] a) G. Nam, J. Park, M. Choi, P. Oh, S. Park, M. G. Kim, N. Park, J. Cho, J.-S. Lee, *ACS Nano* **2015**, *9*, 6493; b) J. Park, M. Park, G. Nam, J.-s. Lee, J. Cho, *Adv. Mater.* **2015**, *27*, 1396; c) J. Fu, D. U. Lee, F. M. Hassan, L. Yang, Z. Bai, M. G. Park, Z. Chen, *Adv. Mater.* **2015**, *27*, 5617; d) Y. Xu, Y. Zhang, Z. Guo, J. Ren, Y. Wang, H. Peng, *Angew. Chem.* **2015**, *127*, 15610; e) Y. Xu, Y. Zhang, Z. Guo, J. Ren, Y. Wang, H. Peng, *Angew. Chem. Int. Ed.* **2015**, *54*, 15390; f) J. Zhang, Z. Zhao, Z. Xia, L. Dai, *Nat. Nanotechnol.* **2015**, *10*, 444.

[6] a) Y. Jin, F. Chen, *Electrochim. Acta* **2015**, *158*, 437; b) J. W. D. Ng, M. Tang, T. F. Jaramillo, *Energy Environ. Sci.* **2014**, *7*, 2017; c) H.-W. Liang, X. Zhuang, S. Brüller, X. Feng, K. Müllen, *Nat. Commun.* **2014**, *5*, 4973; d) B. Li, D. Geng, X. S. Lee, X. Ge, J. Chai, Z. Wang, J. Zhang, Z. Liu, T. A. Hor, Y. Zong, *Chem. Commun.* **2015**, *51*, 8841; e) X. Liu, M. Park, M. G. Kim, S. Gupta, X. Wang, G. Wu, J. Cho, *Nano Energy* **2015**, DOI: 10.1016/j.nanoen.2015.11.030.

[7] a) K. Gong, F. Du, Z. Xia, M. Durstock, L. Dai, *Science* **2009**, *323*, 760; b) S. Chen, J. Duan, J. Ran, M. Jaroniec, S. Z. Qiao, *Energy Environ. Sci.* **2013**, *6*, 3693; c) D. Geng, N. Ding, T. A. Hor, Z. Liu, X. Sun, Y. Zong, *J. Mater. Chem. A* **2015**, *3*, 1795.

[8] L. Dai, Y. Xue, L. Qu, H.-J. Choi, J.-B. Baek, *Chem. Rev.* **2015**, *115*, 4823.

[9] a) M. Prabu, P. Ramakrishnan, S. Shanmugam, *Electrochem. Commun.* **2014**, *41*, 59; b) G. S. Park, J.-S. Lee, S. T. Kim, S. Park, J. Cho, *J. Power Sources* **2013**, *243*, 267; c) Z. Chen, A. Yu, D. Higgins, H. Li, H. Wang, Z. Chen, *Nano Lett.* **2012**, *12*, 1946; d) Y. Liang, Y. Li, H. Wang, J. Zhou, J. Wang, T. Regier, H. Dai, *Nat. Mater.* **2011**, *10*, 780; e) X. Liu, M. Park, M. G. Kim, S. Gupta, G. Wu, J. Cho, *Angew. Chem.* **2015**, *127*, 9790; f) X. Liu, M. Park, M. G. Kim, S. Gupta, G. Wu, J. Cho, *Angew. Chem. Int. Ed.* **2015**, *54*, 9654; g) V. M. Dhavale, S. Kurungot, *ACS Catal.* **2015**, *5*, 1445; h) D. Liu, X. Zhang, Z. Sun, T. You, *Nanoscale* **2013**, *5*, 9528; i) G. Nam, J. Park, S. T. Kim, D.-B. Shin, N. Park, Y. Kim, J.-S. Lee, J. Cho, *Nano Lett.* **2014**, *14*, 1870; j) X. Zhuang, D. Gehrig, N. Forler, H. Liang, M. Wagner, M. R. Hansen, F. Laquai, F. Zhang, X. Feng, *Adv. Mater.* **2015**, *27*, 3789; k) X. Zhuang, F. Zhang, D. Wu, N. Forler, H. Liang, M. Wagner, D. Gehrig, M. R. Hansen, F. Laquai, X. Feng, *Angew. Chem.* **2013**, *125*, 9850; l) X. Zhuang, F. Zhang, D. Wu, N. Forler, H. Liang, M. Wagner, D. Gehrig, M. R. Hansen, F. Laquai, X. Feng, *Angew. Chem. Int. Ed.* **2013**, *52*, 9668.

[10] a) T. Y. Ma, J. Ran, S. Dai, M. Jaroniec, S. Z. Qiao, *Angew. Chem.* **2015**, *127*, 4729; b) T. Y. Ma, J. Ran, S. Dai, M. Jaroniec, S. Z. Qiao, *Angew. Chem. Int. Ed.* **2015**, *54*, 4646; c) G.-L. Tian, Q. Zhang, B. Zhang, Y.-G. Jin, J.-Q. Huang, D. S. Su, F. Wei, *Adv. Funct. Mater.* **2014**, *24*, 5956; d) R. M. Yadav, J. Wu, R. Kochandra, L. Ma, C. S. Tiwary, L. Ge, G. Ye, R. Vajtai, J. Lou, P. M. Ajayan, *ACS Appl. Mater. Interfaces* **2015**, *7*, 11991; e) J. Shui, F. Du, C. Xue, Q. Li, L. Dai, *ACS Nano* **2014**, *8*, 3015.

[11] R. Li, Z. Wei, X. Gou, *ACS Catal.* **2015**, *5*, 4133.

[12] a) L. Dai, D. W. Chang, J.-B. Baek, W. Lu, *Small* **2012**, *8*, 1130; b) T. Chen, L. Dai, *J. Mater. Chem. A* **2014**, *2*, 10756.

[13] a) J. Zhu, S. Wei, X. Chen, A. B. Karki, D. Rutman, D. P. Young, Z. Guo, *J. Phys. Chem. C* **2010**, *114*, 8844; b) D.-J. Liaw, K.-L. Wang, Y.-C. Huang, K.-R. Lee, J.-Y. Lai, C.-S. Ha, *Prog. Polym. Sci.* **2012**, *37*, 907.

[14] Y. Cheng, L. Huang, X. Xiao, B. Yao, L. Yuan, T. Li, Z. Hu, B. Wang, J. Wan, J. Zhou, *Nano Energy* **2015**, *15*, 66.

[15] F. Su, C. K. Poh, J. S. Chen, G. Xu, D. Wang, Q. Li, J. Lin, X. W. Lou, *Energy Environ. Sci.* **2011**, *4*, 717.

[16] W. Luo, B. Wang, C. G. Heron, M. J. Allen, J. Morre, C. S. Maier, W. F. Stickle, X. Ji, *Nano Lett.* **2014**, *14*, 2225.

[17] C. Bommier, R. Xu, W. Wang, X. Wang, D. Wen, J. Lu, X. Ji, *Nano Energy* **2015**, *13*, 709.

[18] X. Lu, W.-L. Yim, B. H. R. Suryanto, C. Zhao, *J. Am. Chem. Soc.* **2015**, *137*, 2901.

[19] a) Y. Gorlin, T. F. Jaramillo, *J. Am. Chem. Soc.* **2010**, *132*, 13612; b) Y. Zhan, G. Du, S. Yang, C. Xu, M. Lu, Z. Liu, J. Y. Lee, *ACS Appl. Mater. Interfaces* **2015**, *7*, 12930.

[20] a) Y. Zhao, R. Nakamura, K. Kamiya, S. Nakanishi, K. Hashimoto, *Nat. Commun.* **2013**, *4*, 2390; b) S. Chen, J. Duan, M. Jaroniec, S.-Z. Qiao, *Adv. Mater.* **2014**, *26*, 2925.

[21] Y. Li, M. Gong, Y. Liang, J. Feng, J.-E. Kim, H. Wang, G. Hong, B. Zhang, H. Dai, *Nat. Commun.* **2013**, *4*, 1805.